Anomalous Diffusive and Electric-field-driven Ion Transport in Boron-Nitride Nanotubes

Semih Cetindag[1], Aaditya Pendse[2], Richard J. Castellano[1], Pavel Rehak[5], Matthew Howard[1], Ku Wang[2], Joshua Yi[1], Robert F. Praino[3], Petr Kral[5*], Liping Liu[4,1], Sangil Kim[2*], Jerry W. Shan[1*]

[1*]Department of Mechanical and Aerospace Engineering, Rutgers University, , Piscataway, 08854, NJ, USA.
[2]Department of Chemical Engineering, University of Illinois at Chicago, , Chicago, 60607, IL, USA.
[3]Chasm Advanced Materials, Applications Development Center, , Canton, 02021, MA, USA.
[4]Department of Mathematics, Rutgers University, , Piscataway, 08854, NJ, USA.
[5]Department of Chemistry, University of Illinois at Chicago, , Chicago, 60607, IL, USA.

*Corresponding author(s). E-mail(s): pkral@uic.edu; sikim@uic.edu; jshan@soe.rutgers.edu;

Abstract

We report on anomalous transport of ions in solution through macroscopic arrays of vertically aligned, surface-charged boron-nitride nanotubes (BNNTs). The 3- and 12-nm-diameter BNNTs revealed two atypical transport phenomena: (i) ultra-fast cation-selective diffusion under concentration gradients that exceeded Fickian diffusion by up to 31-fold and (ii) anomalous relative diffusion rates and ionic conductances for alkali-metal ions (K^+, Na^+, and Li^+) that were opposite to the ordering of their bulk mobilities in solution, and also different from that observed in carbon nanotubes and 2D boron-nitride (BN) nanochannels. The enhanced diffusive transport is shown to result from diffusio-osmosis at the charged BN walls, with the enhancement scaling inversely with pore diameter. The anomalous relative diffusivities for different cations is seen to arise from ion-specific interactions with the charged surface of the BNNTs. These unusual

transport phenomena, as well as the flexible and scalable membrane-fabrication process, may enable ion-selective membranes optimized for "blue" energy conversion, lithium recovery, and other molecular separations. As an example, macroscopic arrays of aligned BNNTs in a salt-concentration gradient produced per-pore osmotic-power densities up 15,300 W/m^2, with energy-conversion efficiencies approaching the theoretical maximum of 50%.

Keywords: Diffusion, conductance, ion selectivity, osmotic energy, nanotubes

1 Main

The rapid and selective transport of ions through nanopores is central to biological systems, as well as a variety of energy-conversion and molecular-separation processes. A variety of remarkable ion-transport phenomena have recently been observed in low-dimensional synthetic nanopores, nanochannels, and nanotubes. For instance, quasi-0D nanopores formed in atomically thin materials have been shown to provide ion selectivity persisting up to 20-nm pore sizes in graphene [1, 2], and enormous osmotic-power generation in nanoporous single-layer MoS_2 [3, 4]. Recent experiments in 2D systems have revealed 3-4-fold-enhanced mobility of protons and cations in 2-nm-deep silica nanochannels [5], and complete ion exclusion accompanied by slower-than-bulk proton diffusion in monolayer water confined between graphene sheets [6].

Among the various low-dimensional systems, 1D nanotubes are particularly intriguing because they offer additional confinement, and can emulate biological channels by having readily functionalizable surfaces and well-defined structures [7, 8]. Recent experiments have found excess ionic conductance in 1.5-nm-diameter metallic carbon nanotubes (CNTs) [9], fast permeation of small ions in 2.2-nm-diameter CNTs [10], and enhanced proton diffusion in 0.8-nm CNTs [11]. For CNTs, this enhanced ion transport has been attributed to a combination of strong confinement, slip-flow enhancement, and ion interactions with the negatively charged carboxyl groups at the CNT entrance, as well as various material drag phenomena [12]. Other studies performed with individual 30-80 nm BNNTs have revealed high surface-charge densities, potentially enabling giant "blue" power generation from natural salinity gradients such as those available at coastal estuaries [13]. Rapid yet selective transport of ions through synthetic nanopores has potential applications in molecular separations, desalination, and energy conversion and storage.

Here, we report on the anomalous diffusion of ions in ultra-narrow BNNTs. We use a novel experimental platform consisting of macroscopic arrays of vertically aligned (VA) nanotubes that serve as through-pores in an impermeable polymer matrix (Fig. 1A). The solution-based, field-assisted fabrication method is scalable and provides flexibility in the use of different types of nanotubes in powder form. To fabricate the nanotube arrays, we aligned BNNTs (3- and 12-nm inner diameter) and CNTs (3-nm inner diameter) with magnetic and electric fields [14–16], respectively. The BNNTs were decorated with iron-oxide nanoparticles to make them magnetically susceptible and thus alignable by a magnetic field (Fig. 1B). The CNTs naturally develop an

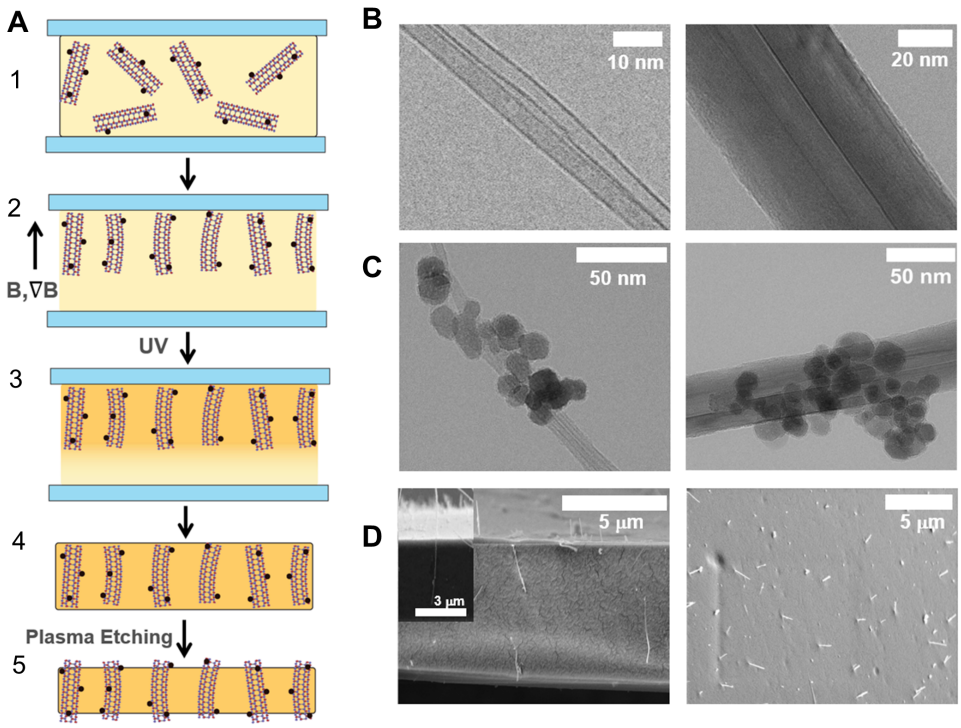

Fig. 1 Vertically aligned (VA-) BNNT and CNT arrays. (a) Solution-based, field-assisted fabrication of VA-BNNT arrays: (1) Magnetically functionalized BNNTs suspended in the liquid oligomer, (2) Magnetic alignment and magnetophoretic deposition of nanotubes, (3) Ultraviolet (UV) curing of urethane oligomer to desired thickness, (4) Extraction of urethane-embedded VA-nanotube array (total area 20 cm^2), (5) Plasma etching to uncap nanotubes. **(b)** Transmission electron microscopy (TEM) image of 12-nm and 3-nm BNNTs. **(c)** BNNTs decorated with Fe_3O_4 nanoparticles. **(d)** Scanning electron microscopy (SEM) image showing aligned BNNTs in, and protruding from, the cross-section of the urethane matrix. Parts of the aligned BNNTs are visible on the cleaved cross-sectional surface, while other portions remain embedded in the matrix. Inset shows a VA-BNNT spanning the cross-section as an ion-conductive channel.

induced electrical dipole under an external electric field as a result of Maxwell-Wagner interfacial polarization [14], so functionalization with nanoparticles was not necessary. The BNNTs or CNTs were then suspended in a liquid urethane prepolymer, aligned and concentrated by the external field, and locked in place by in-situ UV polymerization (Fig. 1D). Plasma etching was then used to remove excess polymer and uncap nanotubes, yielding permeable arrays of vertically aligned nanotube embedded in a 4-5-μm-thick polyurethane matrix. We mounted and tested 1-cm^2 samples cut from larger, $\sim$ 20-cm^2 nanotube arrays. The open pore densities were 7×10^5 pores/cm^2 for the 3-nm BNNT arrays, 1.7×10^5 pores/cm^2 for the 12-nm BNNT arrays, and 1.7×10^5 pores/cm^2 for the 3-nm CNT arrays. The solution-based, field-assisted fabrication approach is simple, flexible in the types of nanotubes used, and highly scalable being compatible with roll-to-roll processing[15].

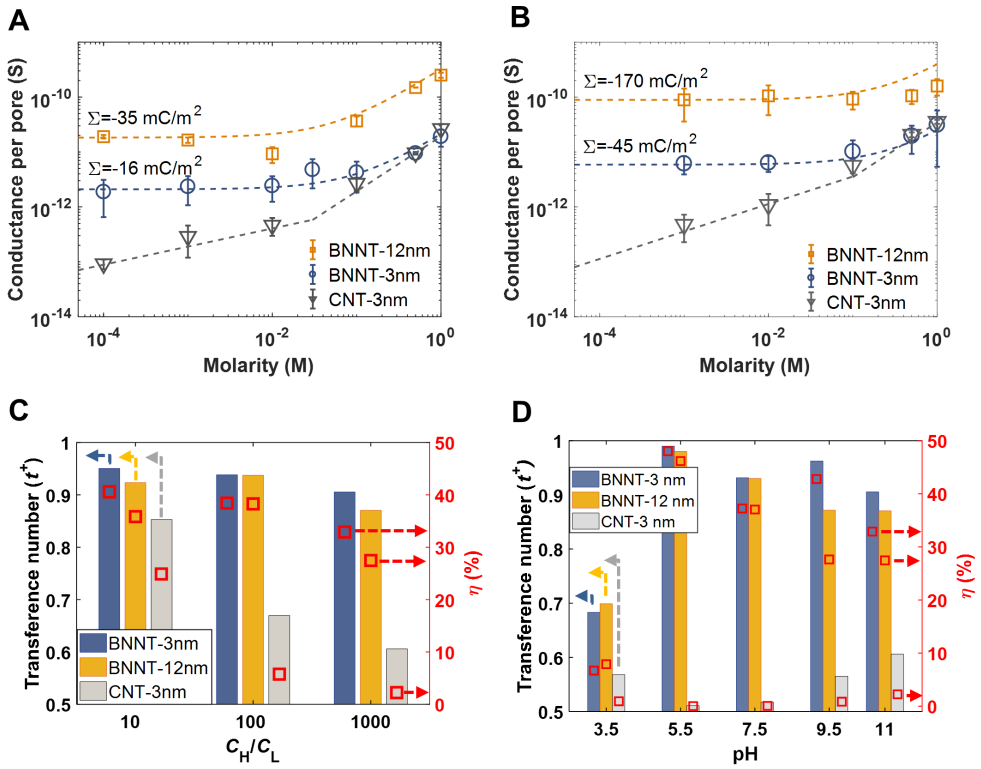

Fig. 2 Surface-dominated conductance and cation-selective transport in BNNTs compared to CNTs. (a) Single-pore conductance and fitted surface-charge density for BNNTs and CNTs in KCl solution at pH=7. **(b)** KCl conductance and surface-charge density at pH=11. **(c)** High K^+ cation selectivity and osmotic-energy-conversion efficiency of BNNT arrays at pH=11, with transference numbers, t^+ ~1 even for C_H=1M. **(d)** Cation selectivity and energy-conversion efficiency for VA-BNNT arrays as a function of pH in a 1mM:1M KCl concentration gradient.

The surface charge of the BN surface can be tuned by adjusting the solution pH, which changes the density of chemi- and physio-sorbed OH^- ions ($BN_3 + H_2O \longleftrightarrow BN_3\text{-}OH^- + H^+$) [17, 18]. At low KCl solution molarities, the VA-BNNT arrays displayed surface-dominated ion transport with a constant conductance that became independent of salt concentration (Fig. 2A-B). Using a model for ionic conductance that accounts for both bulk and surface transport [13],

$$G = \frac{A_{open}}{L_p}\left\{\left[\,10^3 F\left(\mu_{K^+} + \mu_{Cl^-}\right) C_s\right] + \left[\frac{2\mu_{K^+}|\Sigma_w|}{R_p}\right]\right\}, \qquad (1)$$

the BNNT arrays were found to have surface-charge densities of -170 and -45 mC/m^2 at pH=11 for the 12-nm and 3-nm BNNTs, respectively. In the above equation, A_{open}, L_p, and R_p are the total open area, length and radius of the pores, respectively, while F, μ_{K^+}, μ_{Cl^-}, C_s and Σ_w are the Faraday constant, mobilities of potassium

or chlorine ions, solution concentration, and the surface-charge density. At pH=7, the BNNT charge densities decreased to -35 and -16 mC/m^2, respectively. In contrast, the 3-nm CNTs had negligible surface charge. The CNTs, instead of having a constant conductance at low solution molarities, showed a $G \sim C_s^a$ scaling, with exponent $1/3 < a < 1/2$, that is typical of small-diameter CNTs [8], [19].

We then studied diffusive ion transport in the nanotube arrays by immersing the membranes in a salt-concentration gradient and measuring their $I-V$ behavior. For these tests, C_H was varied while C_L was fixed at 1 mM (See Supplementary Information for details). The BNNTs, with their charged surfaces and small diameters, were highly cation-selective, while CNTs of the same size were not. The selectivity was quantified as the ratio of cation-to-total-ion flux, with the transference number, t^+, calculated from the measured osmotic voltage, V_{osm}, as [20]:

$$t^+ = \frac{J^+}{J^+ + J^-} = \frac{1}{2}\left(\frac{V_{osm}}{\frac{RT}{zF} ln\left(\frac{\gamma_H\ C_H}{\gamma_L\ C_L}\right)} + 1\right), \tag{2}$$

where $\gamma_{H,L}$,$C_{H,L}$, R, T, z, are the activity coefficient, ion concentration, gas constant, temperature, and valence, respectively. The subscripts H and L refer to the high- and low-molarity solutions, respectively. A transference number of $t^+ = 0$ or 1 implies complete anion- or cation- selectivity, respectively, while $t^+ = 0.5$ indicates a complete lack of selectivity. Figure 2C-D reveals that the BNNTs possessed excellent K^+ cation selectivity, with t^+ approaching 1. The high selectivity remained constant with increasing C_H, with $t^+ = 0.91$ even for $C_H/C_L = 10^3$ in the 3-nm BNNTs. Cation selectivity persisted for BNNT diameters of 12-nm and C_H=1M, for which the Debye length on the high-concentration side is smaller than pore size. In contrast, 3-nm CNTs showed a rapid decline in selectivity with increasing C_H, which is typical of Donnan (charge-based) exclusion [21]. This is believed to be due to the screening of the charged groups at the CNT tips as salt concentration increases. Thus, despite their identical crystallographic structure and diameter, the 3-nm BNNTs and CNTs showed very different ion selectivity as a result of their different surface-charge density, and distribution thereof.

Intriguingly, measurements of ion transport in these BNNTs revealed atypical absolute rates of cation diffusion. As seen in Fig. 3A, the experiments showed strikingly enhanced absolute rates of K^+, Na^+, and Li^+ diffusion over Fickian diffusion in these BNNT pores. For Li^+, the per-pore fluxes were 21-fold and 31-fold higher than those expected for bulk diffusion in the 3-nm and 12-nm-BNNTs, respectively. In comparison, the previously reported cation flux for a single 80-nm BNNT under the same KCl concentration gradient revealed an enhancement of 1.6-fold [13]. The order-of-magnitude larger enhancement in cation-diffusion rates for the present BNNTs is believed to be due to their smaller diameter, which increases the importance of surface transport relative to bulk diffusion, as will be discussed in more detail later. The anomalous cation mobility in BNNTs is also striking compared to CNTs of the same size (3 nm), as well as previous 4-nm-deep 2D silica nanochannels [20], both of which showed no enhancement in diffusive cation flux over bulk rates ($J^+/J^+_{Fickian} < 1$). It should be noted that these calculations of cation-transport enhancement in the BNNT arrays are inherently conservative because they come from the measured current and

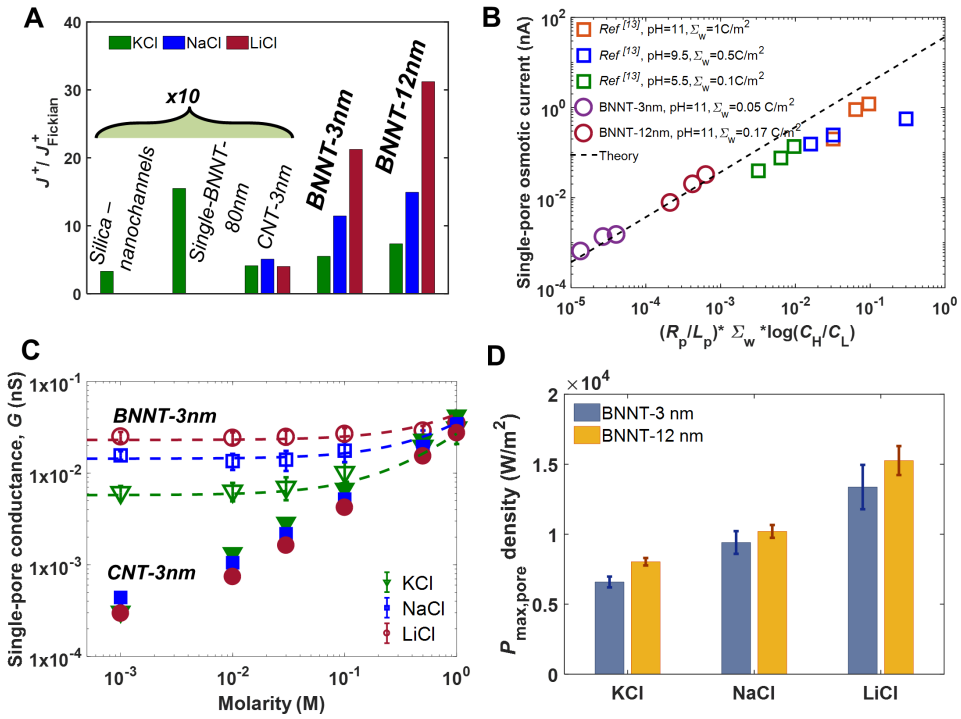

Fig. 3 Enhanced, anomalous diffusion of different cations in BNNTs. (a) Diffusion rates of different cations in various nanotubes compared to bulk diffusion expectations. Note that transport rates in 4-nm silica nanochannels [20], 3-nm CNTs, and the single 80-nm BNNT [13] are multiplied 10-fold for clarity, *i.e*, they more than an order of magnitude lower than that in the 3- and 12-nm BNNTs. **(b)** Scaling of per-pore current compared to diffusio-osmotic predictions of 3. The 3- and 12-nm BNNT arrays of the present work are compared with single BNNTs of different pore diameter, length, and surface charge density in KCl solutions of different pH and concentration gradients. **(c)** Per-pore conductance for 3-nm-BNNT and CNT arrays for various salts at pH=11. **(d)** Per-pore power density for 1mM:1M concentration difference for different salts at pH=11.

assume that only cations are diffused through the nanotubes, *i.e*, $I = q\,(J^+ - J^-) \cong qJ^+$. Since the BNNTs showed transference numbers close to, but not exactly 1, (2C-D), the actual transport rate of cations is likely slightly greater than shown in Fig. 3A.

To interpret the enhanced absolute rate of cation diffusion, we first considered a continuum-level explanation based on the osmotic-pressure-driven flux of concentrated cations in 1D nanotubes. To screen the measured surface-charge density of Σ_w =-170 mC/m^2 on the 12-nm-BNNT surface, for example, the average cation concentration in the electrical double layer ($\lambda_D \approx$ 10nm) would be $\Sigma_w/\lambda_D \approx$ 0.2 M, two orders of magnitude higher than the bulk concentration on the low-molarity side (C_L=1 mM). An osmotic-pressure gradient can drive the concentrated cations in the double layer,

resulting in a diffusio-osmotic current [13]:

$$I_{OSM,total} = N\frac{2\pi R_p}{L_p}\left|\Sigma_w\right|\frac{k_B T}{\eta\lambda_B} log\left(\frac{C_H}{C_L}\right), \tag{3}$$

where N is the pore number, R_p is the pore radius, L_p is the pore length, η is the viscosity, and λ_B is the Bjerrum length.

We have compared this prediction with the measured (per-pore) osmotic current for KCl in the present BNNT arrays, as well as previous single BNNTs of larger diameters [13]. Accounting for the order-of-magnitude differences in pore radius R_p and length L_p, as well as surface-charge density Σ_w, the per-pore osmotic currents for the diffusion of K^+ cations compare well between the predictions of Eqn. 3 and measurements of the present work on 3-nm and 12-nm BNNTs, as well as with previous measurements with a single 80-nm BNNT [13]. (see Supplementary Information for details). The agreement shown in Fig. 3B between the data and theory over three orders of magnitude in osmotic current, with no adjustable parameters, is strong evidence for diffusio-osmosis being the dominant mechanism for enhanced, cation-selective transport in the charged BNNTs. Moreover, the scaling agreement for K^+ diffusion between the previous single BNNTs and the present BNNT arrays suggests that the total osmotic current scales linearly with pore number rather than sub-additively. This linear dependence of conductance on the pore number is different from the expected $N^{1/2}$ scaling for an array of closely spaced pores (when the interpore distance is closer than $4\sqrt{N}\ R_p^2/\ L_p$, where N is the number of pores) [22]. From Eqn. 3, the enhancement in diffusive current over bulk diffusion can be seen to scale inversely with R_p, *i.e.* is greater in smaller-diameter nanotubes. Overall, the enhanced absolute rates of cation diffusion in the BNNT arrays can be rationalized in a continuum sense as the diffusio-osmosis of concentrated ions in the electrical double layer within the charged pores.

However, the data also revealed an anomalous relative transport of Li^+ and Na^+ compared to K^+ within the 3-nm and 12-nm BNNTs, which cannot be explained by continuum diffusio-osmosis. Figure 3A shows that the apparent diffusion rates of K^+, Na^+, and Li^+ in BNNTs differed by up to 4.2-fold, but in the opposite order to their known mobilities in bulk solution [23], as well as in 2D BN nanochannels [24–27]. Furthermore, the relative diffusion rates of the three different cations in BNNTs also differed from that in 3-nm CNTs. In bulk solution, K^+ has a smaller hydrated size and, thus, a higher diffusivity than Na^+ and especially Li^+. However, in the narrow, charged BNNTs, the diffusive transport of cations was ordered as $J_{Li+} > J_{Na+} > J_{K+}$. Moreover, the faster relative transport of Li^+ and Na^+ compared to K^+ is not limited to concentration-gradient-driven diffusion in the BNNTs, but is also seen in the electric-field-driven ionic conductance. As shown in Fig. 3C, the ionic conductance of the BNNT arrays diverged significantly for KCl, NaCl, and LiCl at low molarities, with LiCl giving the highest conductance for C_s<100mM. In contrast, ionic conductances for 3-nm CNTs pores nearly collapse for the different salt solutions, with only a small difference (KCl having the highest conductance) that is consistent with the difference in hydrated size and bulk mobilities of Li^+, Na^+, and K^+ cations in solution. Thus, the BNNTs, but not CNTs, showed both diffusive and electric-field-driven (conductance)

transport rates that were anomalously enhanced for Li^+ compared to that of Na^+ or especially K^+.

This anomalous opposite-from-bulk ordering of transport rates for Li^+, Na^+, and K^+ in the BNNTs is distinct from what has been previously seen experimentally, and also from what is predicted by conventional models. Standard diffusio-osmosis does not distinguish between different monovalent cations, as can be seen in Eqn. 3. Furthermore, while it is known that differences in anion-to-cation diffusivities can generate an electric field $E_{\text{diff}} = \frac{k_B T}{q} \beta \nabla \log C$, where $\beta \equiv (D^+ - D^-)/(D^+ + D^-)$) that could affect diffusio-osmotic transport; we do not expect this to occur in these small-diameter BNNTs because anions are completely excluded, as seen both experimentally ($t^+ \to 1$ in Fig. 2C and D), and in molecular dynamic simulations. Thus, $\beta \cong 1$ is independent of the salt type, and we would not expect to see salt-specific differences in diffusio-osmotic transport. Moreover, we find the same anomalous ordering of cation transport rates in conductance experiments (Fig. 3C), where the solution molarities are equal on both sides of the BNNTs and transport is driven by an external electric field rather than diffusion. Thus the diffusion electric field does not appear to be able to explain the anomalous relative ordering of diffusion rates of various ions in the BNNTs. Furthermore, the transport-rate ordering that we observe in BNNTs is opposite to that reported by Geim's group for diffusion in angstrom-scale 2D hBN channels, despite the two systems having the same h-BN walls and, presumably, surface properties [24]. For these reasons, the ion-specific diffusion rates and conductances that are observed in BNNTs are quite unexpected.

Our observations indicate that ion transport inside small-diameter BNNTs is strongly affected by ion-specific interactions between the ions and the walls of the BNNTs. Charged OH- groups on the h-BN wall can hinder the motion of cations in the axial direction. For simplicity, we may model this local interaction by an additional potential whose depth Q varies for different species, *e.g.*, Li^+ vs. K^+. The fraction of cations trapped in the energy wells can be shown to be:

$$f = \frac{1}{1 + \alpha_1 e^{-Q/K_B T}} \tag{4}$$

and, by Kramer's theory [28, 29], the effective mobility of cations trapped in the wells is then:

$$\mu_B^+ = \mu^+ \alpha_2 e^{-Q/k_B T}, \tag{5}$$

where α_1 and α_2 are dimensionless constants that depend on the detailed profile of the energy barrier. Small differences in the surface-interaction potential can thus have exponential impact on the effective diffusivity and conductance for different species. Additional molecular dynamics and computational quantum-chemistry investigations in this direction are underway.

Although considerable challenges remain in terms of scale-up and increasing areal power density, the fast, ion-selective transport in VA-BNNT arrays could potentially enable applications such as electricity generation by harvesting "blue" energy from concentration gradients such as those that occur at natural estuaries [7, 30–32] Since per-pore power density scales as Σ_w / R_p (see Eqn. 2 & Fig. 3B), decreasing the pore size significantly increases the power density over that of previous, larger-diameter

BNNTs. As shown in Fig 3D and Fig. S16, the 3- and 12- nm BNNT arrays show per-pore power densities exceeding 10,000 W/m^2 for 1mM:1M NaCl solutions, and 15,000 W/m^2 for KCl. This compares favorably with the 4,000 W/m^2 found for the single 80-nm BNNT studied previously under the same conditions [13]. The osmotic power increased linearly with surface-charge density (which was varied by changing pH), as well as with the log of the concentration gradient across the membrane, as seen in Figs. S14-S15. These scalings are consistent with the diffusio-osmotic predictions of Eqn. 2. As a result of their high cation selectivity, the BNNT arrays had osmotic-energy conversion efficiencies $\eta_{max} = \frac{\left(2t^+ - 1\right)^2}{2}$ [20] approaching the maximum possible 50%, as shown in 2C-D (higher efficiencies are only possible for pairs of cation- and anion-selective membranes). The conversion efficiencies of the BNNTs were notably higher than the <10% of CNTs of the same diameter, as well as 4-nm-high 2D silica nanochannels (8%) [20], and 5-nm-diameter nanopores in MoS_2 nanosheets (17.6%) [3].

Moreover, the solution-based, field-assisted fabrication method is inherently compatible with roll-to-roll processing and enables the scale-up of the VA-BNNT arrays. With 1-cm^2 arrays of the current work, the overall current was 10^4-fold greater (10 μA *vs.* 1 nA) than that in the single 80-nm BNNT of previous work [13]. As a proof of concept, we have powered a calculator, watch, and LED using a stack of eight 1-cm^2 BNNTs arrays in series (Fig. S20 & Supplementary Movies S4-6). Further improvements in areal power density and total power of the array could be made by increasing the array size, pore density, and open-pore percentage, as presently only a portion of the BNNTs have etched-open caps. It may also be of interest to take advantage of the anomalously enhanced transport rate for certain cations in BNNT pores to recover or concentrate species such as lithium from mixed salt solutions.

These results show that ion transport in narrow BNNTs is enhanced with respect to bulk and highly selective for specific cations. The marked difference in both ionic diffusion and conductance between BNNTs and CNTs, the latter of which show negligible osmotic power generation but have a significant enhancement in water flow [8, 15, 33, 34], highlight the subtle but important differences in surface charge and hydrodynamic slip that govern ion transport in otherwise similar, atomically perfect 1D nanotubes. The quasi-1D confinement of ions in BNNTs also appears to be fundamentally different from 2D confinement in BN nanochannels, as seen in the different ordering of ionic conductance for various alkali metal ions between the two systems. Due to the surface-dominated transport in 1D BNNTs, the overall transport of cations is enhanced by more than an order of magnitude over bulk values. Moreover, species-specific interactions between cations and the charged h-BN surface cause the relative transport rates of different alkali-metal ions to be anomalous, with Li^+ transported 4-7-fold faster than K^+, for instance. These unexpected phenomena, together with the scalable and flexible fabrication technique that enables macroscopic membranes with a variety of nanotube pores, may provide opportunities to better understand fundamental ion transport in 1D nanochannels, and indicate a possible path for the rational design of ion-selective membranes optimized for "blue" energy conversion, desalination, lithium recovery, and other molecular separations.

2 Methods

2.1 Functionalized boron nitride nanotubes

Multi-walled (ID=12 nm, Naieel Technology, South Korea) and few-walled (ID=3nm, BNNT, LLC USA) boron-nitride nanotubes were functionalized with iron-oxide nanoparticles using electrostatic adsorption arising from the difference of surface charge in these two materials. Nanotube inner diameters were measured using a series of TEM images. Figure S1 shows the inner-diameter distributions of the 3- and 12-nm BNNTs, as well as the 3-nm CNTs used in this study. For the larger BNNTs, the estimated average inner diameter was 12 nm with a standard deviation of 2 nm, while for smaller BNNTs, the average inner diameter was 3 nm with a standard deviation of 0.9 nm. The CNTs had a mean diameter of 3 nm with a standard deviation of 1 nm. Extended Data Figure A2 show Raman spectra and diameter distributions of the different nanotubes.

Typically, a suspension of nanotubes was prepared in isopropanol solution (ACS reagent, $\geq$99.5%, Sigma-Aldrich) at a concentration of a 1mg/mL. Following 15 min. of bath sonication at a controlled temperature of 20 ^{0}C, the IPA was evaporated and replaced with deionized water. The aqueous suspension of BNNTs was then bath sonicated for another 10min, followed by a brief 30s tip sonication. Next, 40μL of ferrofluid (EMG 605 Ferrotec USA Corporation) was added to 10 mL of the aqueous BNNT suspension. The d=10 nm iron-oxide nanoparticles (3.9 vol% in a waterbased ferrofluid) were cationic-surfactant coated. This caused the positively charged magnetic nanoparticles to electrostatically adsorb to the negatively charged BNNTs. This adsorption typically takes 10 minutes and reached a maximum after $\sim$3 hours. Successful functionalization of the nanotubes can be observed in their magnetophoretic response to the magnetic field of a rareearth magnet, as seen in Extended Data Fig A3 and Supplementary Information Fig 7. Functionalization of nanotubes was completed by leaving them overnight in suspension, washing nanotubes with DI water and filtering out the extra deionized water using a PTFE filter with 0.2 μm pore size. After the complete removal of water by evaporation, dry functionalized nanotubes were stored for further steps in membrane fabrication.

It is important to note that decoration with iron-oxide nanoparticles is only observed on the outside surface of the nanotubes and that the nanoparticles do not clog the inner nanochannels of the BNNTs. This was verified by a series of TEM images of the 12-nm-diameter BNNTs shown in Extended Data Fig A1. By tilting the microscope stage around the nanotube axis, the 3-dimensional position of the nanoparticles can be determined. The sequence of TEM images shows that the magnetite particles were on the outside of the nanotubes. Similarly, successful functionalization on the outside of the 3-nm-diameter BNNTs is also observed in Extended Data Fig A1. Analysis of the TEM images show that the functionalized nanotubes cover 1-3% of the BNNT surface area. The field-induced alignment of functionalized multi-walled boron-nitride nanotubes under a known magnetic field was also observed with a high-speed CCD camera (pco.edge CMOS, PCO AG) attached to an inverted optical microscope (Model IX71, Olympus Inc) with a 100X oil-immersion objective. Movies S1-S3 show

videos of the alignment of individual, liquid-suspended BNNTs in magnetic fields of different strength and direction.

2.2 Alignment and magnetophoretic deposition of functionalized BNNTs

To fully benefit from the incorporated boron-nitride nanotubes, nanotubes were vertically aligned and concentrated with an applied magnetic field prior to curing of the polymer matrix. Using rareearth magnets, a 1000G magnetic field was applied for 10 min to the mixture of functionalized nanotubes and liquid oligomer. A urethane thin film with vertically aligned BNNTs was UV cured immediately after the magnetic field is removed. We compared the experimentally measured alignment rate of functionalized nanotubes with theoretical predictions. The magnetic-alignment energy of individual nanotubes can be expressed as [35],

$$U(\theta) = \frac{2\pi}{3}\left[\left(\frac{L}{2}+\Delta\right)\left(\frac{D}{2}+\Delta\right)^2 - \left(\frac{L}{2}\right)\left(\frac{D}{2}\right)^2\right]\mu_0\frac{\chi_p^2}{\chi_p+1}H_0^2 sin^2\theta, \quad (6)$$

In Eq. 6, L and D represent the length and diameter of nanotubes (modeled as prolate spheroids), Δ and χ_p represent iron-oxide particle diameter and magnetic susceptibility and H is the applied magnetic-field strength. The magnetic torque of an individual nanotube is predicted to be [35],

$$|T_m| = -\frac{dU_m}{d\theta} = \frac{2\pi}{3}\left[\left(\frac{L}{2}+\Delta\right)\left(\frac{D}{2}+\Delta\right)^2 - \left(\frac{L}{2}\right)\left(\frac{D}{2}\right)^2\right]\mu_0\frac{\chi_p^2}{\chi_p+1}H_0^2 sin2\theta \quad (7)$$

As the nanotubes rotate into alignment with the applied magnetic-field direction, the magnetic torque is balanced by the viscous torque on the cylinder. In the low-Reynolds-number limit, the torque balance is $|T_m| + \zeta_v\Omega = 0$ in which T_m, ζ_v and Ω (rad/s) correspond to magnetic torque, hydrodynamic rotational-friction constant, and alignment rate, respectively. Thus, the theoretical maximum alignment rate of an individual nanotube, taking place at $\theta = \frac{\pi}{4}$, in which θ is the orientation angle between the applied H-field direction and the particle's long axis, can be expressed as,

$$\Omega = \frac{|T_m|}{\zeta_v} = \frac{\frac{2\pi}{3}\left[\left(\frac{L}{2}+\Delta\right)\left(\frac{D}{2}+\Delta\right)^2 - \left(\frac{L}{2}\right)\left(\frac{D}{2}\right)^2\right]\mu_0\frac{\chi_p^2}{\chi_p+1}H_0^2}{\frac{\pi\eta L^3}{3(ln(L/D)-0.8)}}, \quad (8)$$

Eq. 8 predicts that the nanotube alignment rate scales with the field strength as H_0^2, as well as with nanotube dimensions as $ln(L/D)/L^2$, assuming the nanoparticles are covering the nanotubes outer surface homogeneously. Fig. A4 shows a superimposed image sequence of a nanotube rotating into alignment with a horizontal magnetic field. Using such a sequence of recorded images and fitting the orientation angle, θ, to an exponential decay function of the form [16, 36], we can extract the maximum alignment rate, Ω_{max}, for different nanotube geometries and magnetic-field strengths.

Fig. A5 shows that the predictions of rotation rate scaling as H_0^2 and $ln(L/D)/L^2$ are in good agreement with the experimental data. The effect of applied field strength on a nanotube's alignment is illustrated in Movies S1 and S2, which show the same nanotube aligning at 240G and 43G, respectively. The agreement between theory and measured alignment rates for nanotubes of different length, as shown in Fig. A5B, also suggests relatively homogeneous functionalization of magnetite particles along the surface of the nanotubes. Movie S3 shows the magnetic alignment of nanotubes in DI water solution with an initially horizontal, followed by vertical, magnetic fields.

2.3 Fabrication of boron nitride nanotube arrays

To create arrays of vertically aligned-(VA-) BNNTs embedded in a polymer matrix, functionalized nanotubes were dispersed in a UV-curable liquid polymer, specifically an acrylated polyurethane oligomer, SU-710 (Soltech, LTD). A photoinitiaor (Darocur 1173, BASF Corp.) was mixed with the liquid oligomer at a 5% vol. concentration. The mixture of photoinitiator and liquid oligomer was bath sonicated at 50 ^{0}C for 30 min and mixed with a vortex mixer for another 10 min before the introduction of nanotubes. Magnetically functionalized nanotubes were mixed in the oligomer mixture at a concentration of 1mg/ml and bath sonicated at 50 ^{0}C for 30 min. The dispersed nanotube-liquid oligomer mixture was then placed in a fluidic set-up consisting of two ITO-quartz slides with high transmission of UV light (OPCO Laboratory, Inc), separated by a 200μm thick double-sided-tape spacer.

A 285 nm UV lamp illuminated the urethane oligomer through the UV-transparent ITO slides for a certain duration, typically few seconds. The thickness of the cured matrix was varied by changing the duration of UV exposure. An initial calibration of thickness versus UV exposure duration was performed to enable curing of the target thickness of the membranes. Before curing of the liquid oligomer, nanotubes were aligned and deposited vertically in the fluidic set-up with a magnetic field, as discussed in next section. SEM images of the vertically aligned BNNTs protruding from the polymer surface are shown in Fig 1D of the manuscript as well as Supplementary Information Fig 8. The uncured, excess liquid oligomer on top of the cured film was then washed away by spraying acetone and deionized water. After the ~ 20 cm^2 BNNT arrays were fabricated, they were cut into smaller ~ 1 cm^2 sections and mounted on a 200 μm thick polymer supports for plasma etching and testing.

2.3.1 BNNT array etching and thickness measurement protocol

To eliminate the excess polymer and uncap the deposited boron-nitride nanotubes, a plasma-etching protocol was introduced. For etching, 1:1 (% mass flow rate) SF_6-O_2 gas was used in a plasma-etching system (March Instruments Inc, PX250). Among these gases, SF_6 etches boron-nitride [37, 38], while O_2 targets the excess polymer matrix. To check the effect of SF_6 on the hexagonal boron-nitride, exfoliated h-BN platelets were etched and examined under SEM, as seen Fig.S9. To reduce sample heating and defect generation in the cured polymer matrix, etching was done in multiple 1 min cycles at a plasma power of 100 W for each side until the target open-pore

number was reached. After each cycle, measurements were made of the ion conductance and osmotic-power generation of the arrays to check for any possible defects. Typically, membranes with starting thickness of 6.0 μm thickness were etched down to 5.0 μm after 6 or 7 rounds of plasma etching on each side. Membrane thicknesses were measured using a thin-film measurement system employing spectral reflectance (Filmetric F20-EXR) with wavelength range of 400-1700 nm. Before thickness measurement, light-exposure conditions were calibrated for SiO_2 on Si wafers with known thickness.

2.3.2 Verification of Total Open Area and Pore Number Estimation

The total open pore area was measured using ion-conductance measurements, and verified with N_2-gas-permeation and Au exclusion tests. The bulk conductance at high molarity (0.5-1 M KCl) gives the total open pore area, while the surface-dominated conductance at low molarities gives the surface charge density of the pores. In high-molarity solutions, the surface-charge contribution to ion conductance in the second term of Eq. 1 can be neglected. In Eq. 1, $A_{open,p}, L_p, R_p, F, \mu_{K+}, \mu_{Cl-}, C_s$ and Σ_w correspond to total open area of the pores, thickness of the membrane (m^{-1}), radius of nanotubes (m^{-1}), Faraday constant ($C.m^{-1}$), mobilities of potassium and chlorine ions ($7.62x10^{-8}$ and $7.91x10^{-8} m^2 V^{-1} s^{-1}$), solution concentration, and wall surface charge (C/m^2) respectively. The open pore number of the fabricated BNNT arrays can be estimated from the measured conductance, G, at high molarity and the TEM-measured inner radius, R_p, of the nanotubes using,

$$N = \frac{(G_{total}\ L_p)}{\pi R_p^2 10^3 F \left(\mu_K^+ + \mu_{Cl}^-\right) C_s} \tag{9}$$

As previously mentioned, in high-molarity solution (C_S >0.5M), ion conductance is dominated by bulk conductance, which is a linear function of total open area. It is important to note that any additional conductance due to the surface conductance would tend to increase the estimated total pore number (and thus underestimate the generated osmotic power density). Furthermore, since the open pore area is measured individually for each nanotube array, it is also a valuable probe to detect possible defects generated during the array fabrication, or in subsequent plasma etching. Nanotube arrays with defects in the polymer matrix generated during the fabrication process have orders-of-magnitude-higher initial ion conductance prior to any etching, as shown in Fig. S5B. Tears or defects can also originate after fabrication, during plasma etching or handling. In defective nanotube arrays, the osmotic power density is significantly lower, as shown in Fig. S5A.

To further validate the conductance-measured open-pore area, we have also performed N_2-gas-permeation tests as a second, independent way of measuring open-pore area. Gas-flow rates in the Knudsen-flow regime (for pore diameters smaller than the mean free path of the diffusing gas molecules) can be estimated as,

$$Q = N \frac{d^3 \Delta P}{6PL} \sqrt{\frac{2\pi k_B T}{m}} \tag{10}$$

Here, Q is the gas flux through the BNNT-12nm array, N is the number of open BNNT-12nm pores, d is the inner diameter of the nanotubes, ΔP is the pressure difference across the array, P is the atmospheric pressure, L is the thickness of BNNT array, k_B is the Boltzmann constant, T is absolute temperature and m is the molecular weight of the gas. The measured N_2-gas permeance is shown in Fig.S3. Figure S3(C) compares the open areas for three BNNT-12 arrays measured by the N_2-gas-permeation and ion-conductance tests. Typically, the pore areas estimated with ion conductance measurements and N_2-gas permeance agree within 2%-10%.

In addition, to rule out possible defects and further verify the BNNTs are the sole ion transport paths, we have performed pressure-driven Au exclusion experiments across BNNT arrays with 15nm Au nanoparticles. Solutions of 0.025 mg/ml of 15 nm polyethylene-glycol- (PEG-) functionalized Au nanoparticles (NanoComposix, item no. AUGN15-25 M) were injected into the feed side covering the film surface and a pressure of 34.5 kPa was applied. We note that any rejection is expected to be based on size exclusion, as the PEG functionalization of Au particles establishes a low surface charge on the particles. Measured rejection value ($R = 1 - A_p/A_f$), where A_p and A_f are measured permeate and feed absorbances near 522 nm) is 93.4%. We have also tested arrays with defects, and compare successfully fabricated and defective BNNT arrays in Fig.S6 in terms of both Au exclusion and power generation. For the defective-membranes, unintentional defects create extra flow paths in addition to inner surface of nanotubes, resulting in a significantly reduced rejection rate of 54%, and negligible osmotic power generation for 1mM:1M KCl solution at pH=11.

2.4 Current-voltage measurements

Alkali metal ion solutions of KCl, NaCl and LiCl were used as electrolytes in the experiments. All solutions were prepared by dissolving salt in deionized water (resistivity of $\rho = 18.1$ MΩ.cm), followed by a series of dilutions to reach the desired lower molarities. For pH adjustment, KOH (0.1N, Sigma-Aldrich) or HCl (diluted to 1M, Sigma-Aldrich) was added drop-wise. The conductivities of the prepared solutions were measured with a conductivity-meter probe (Oakton Instruments CON6 Acorn series), calibrated with buffer solutions prior to measurements (Hanna Instruments HI 7033 and HI 7031). The pH of the solutions was also measured with a benchtop pH meter (Thermo Scientific STAR A111), again calibrated immediately before the measurements.

Before ionic-current measurements, BNNT arrays were pre-wetted by initial soaking in a 25% ethanol/75% water mixture for 5min. The BNNT arrays were then soaked/rinsed in deionized water for another 15min, and then presoaked for 30 min in a salt solution. The membranes are presoaked in the low-molarity-side salt solution for osmotic-current measurements, and in a solution of the desired molarity for ionic-conductance measurements. For ionic-current measurements, the fabricated arrays were clamped between two reservoirs with Viton O-rings in a custom-made two-reservoir electrochemical cell enclosed in a Faraday cage. Chlorinated Ag/AgCl wire electrodes (A&M Systems, Catalog# 531500) were used in both reservoirs to apply trans-membrane potential and record the current. When necessary, electrodes were cleaned with nitric-acid solution (HNO_3, 70%, Sigma Aldrich) and re-chlorinated

by soaking in NaClO or electroplating in NaCl (3M) solutions. Ionic currents across the BNNT arrays were recorded at various pH conditions and electrolyte concentrations using a Gamry Reference 600+ with pA resolution. For I-V recordings, the applied voltage was scanned over a $\pm$0.3V range, of which $\pm$ 0.2V is used to extract data for calculations. For the successfully fabricated and tested membranes, I-V recordings were linear within the applied voltage range. To verify the experimental protocols, a series of control measurements of ionic conductance were performed with d=20μm single-micropore SiN_x membranes (Norcada, NTPR005A-C20) and track-etched polycarbonate membranes of known pore size and number.

Supplementary information. Available in the online version of the paper.

Acknowledgments. This work was supported by NSF-CMMI/GOALI Grant #1762913.

Author contributions. J.W.S., S.K., R.F.P. & S.C. conceptualized the project. K.W. characterized the BNNTs and CNTs. S.C. carried out the BNNT-array fabrication and characterization, ion-transport experiments and data analysis. R.J.C. performed CNT-array fabrication and characterization. P. K and P. R. carried out molecular-dynamics simulations, with input from all authors. L.L. provided theoretical analysis of the effect of attractive potentials on diffusion near walls. J.W.S. and S.C. analyzed data and wrote the manuscript, with input from all authors. Competing interests: The authors declare no competing interests.

Data and materials availability. All data are in the main text, extended data or supplementary information.

Appendix A Extended data figures and tables

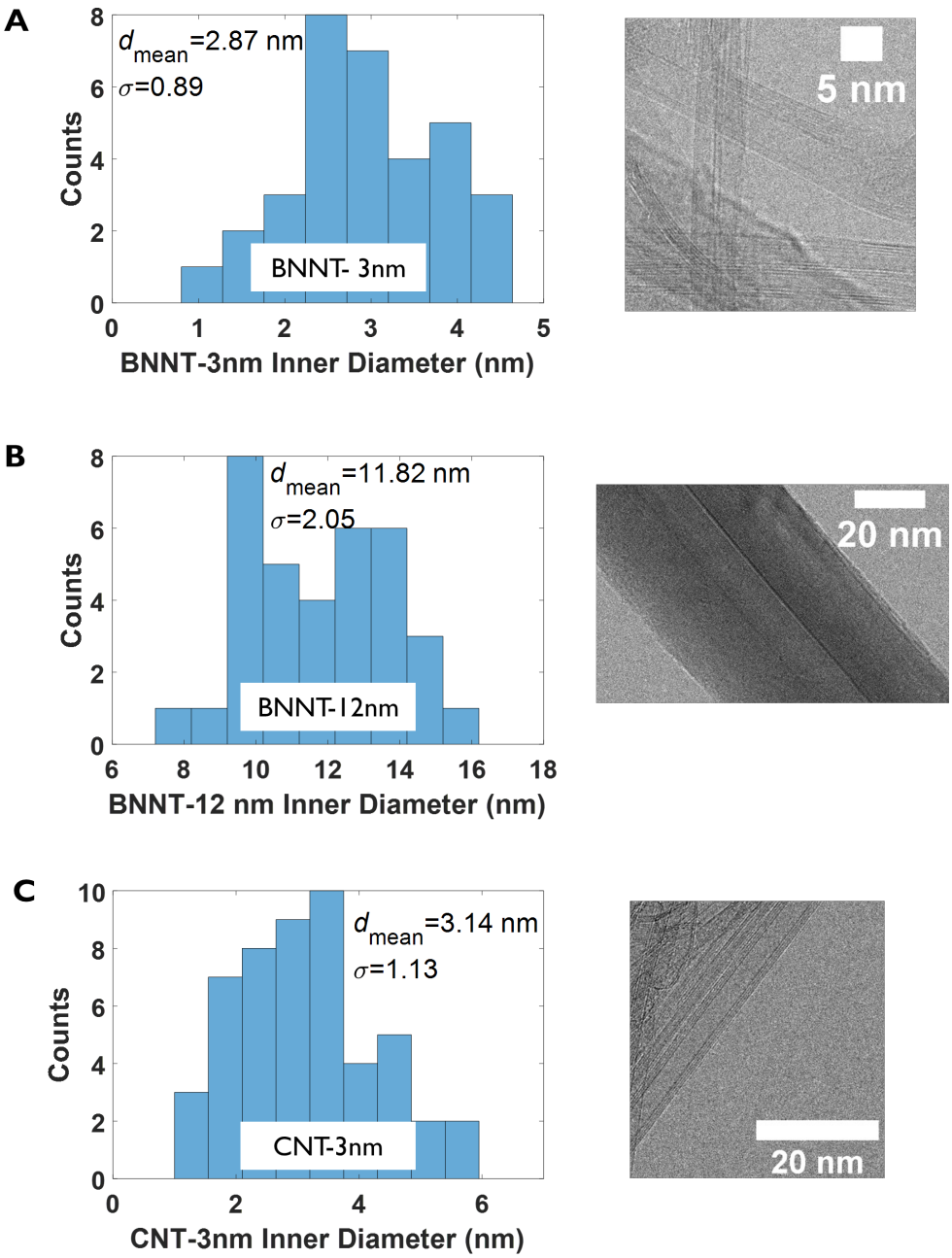

Fig. A1 Inner diameter distribution of (a) 3-nm BNNTs (d∼3nm± 0.9nm) **(b)**12-nm BNNTs (d∼12nm± 2nm) **(c)** 3-nm CNTs (d∼3nm±1nm).

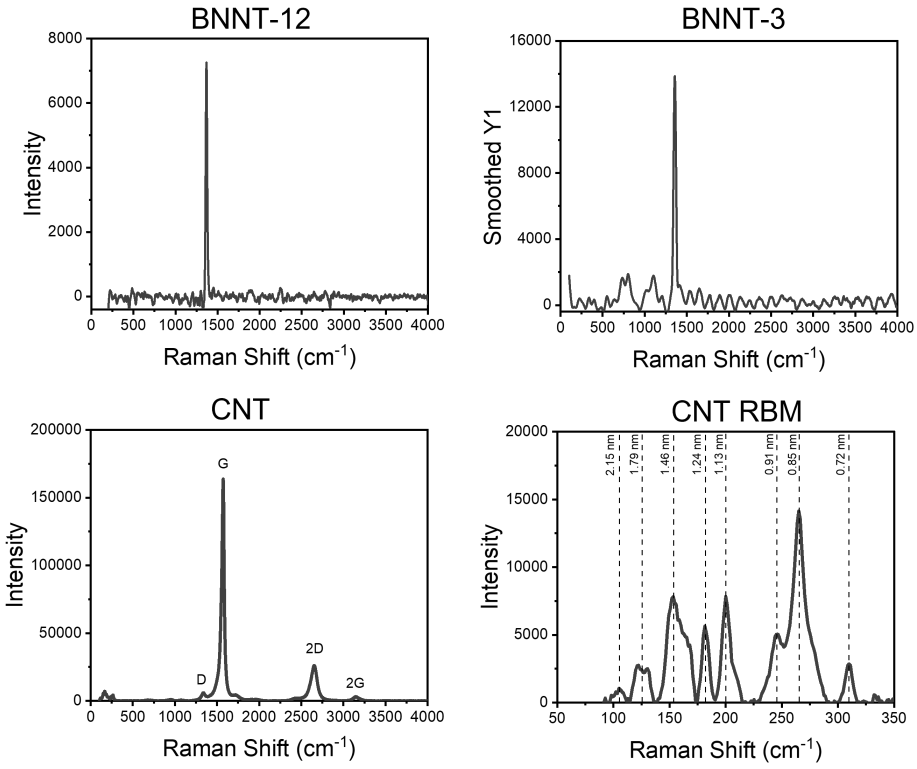

Fig. A2 Raman spectra of 3- and 12-nm BNNTs, and 3-nm CNTs

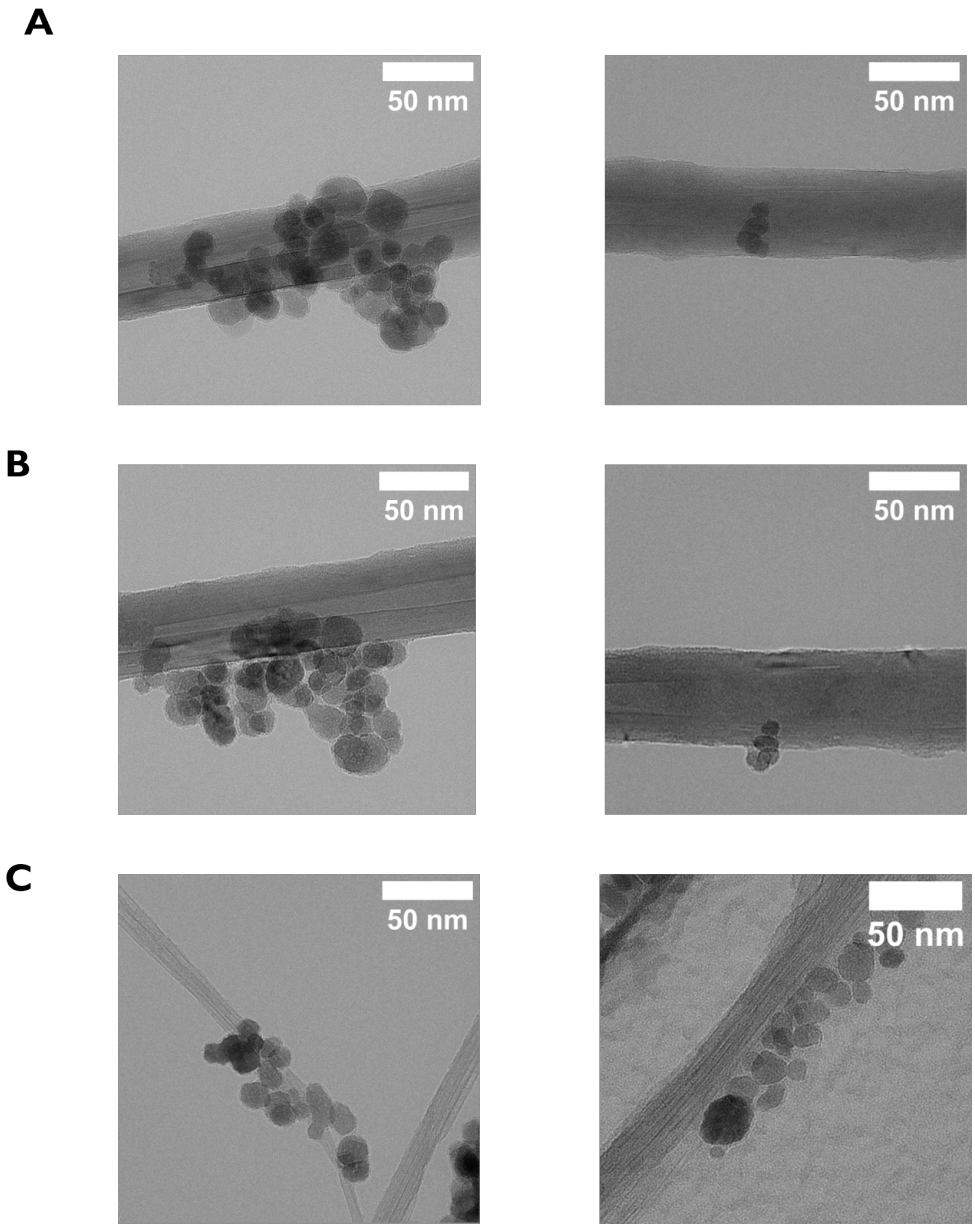

Fig. A3 Functionalized 12-nm and 3-nm BNNTs with iron-oxide nanoparticles (a) TEM images of nanotubes after functionalization **(b)** Tilted stage with 45 degree has changed the position of both the magnetite and host nanotubes suggesting the nanoparticles reside on the outer surface of nanotubes 12-nm BNNTs, **(c)** TEM images of 3-nm BNNTs functionalized with iron-oxide nanoparticles.

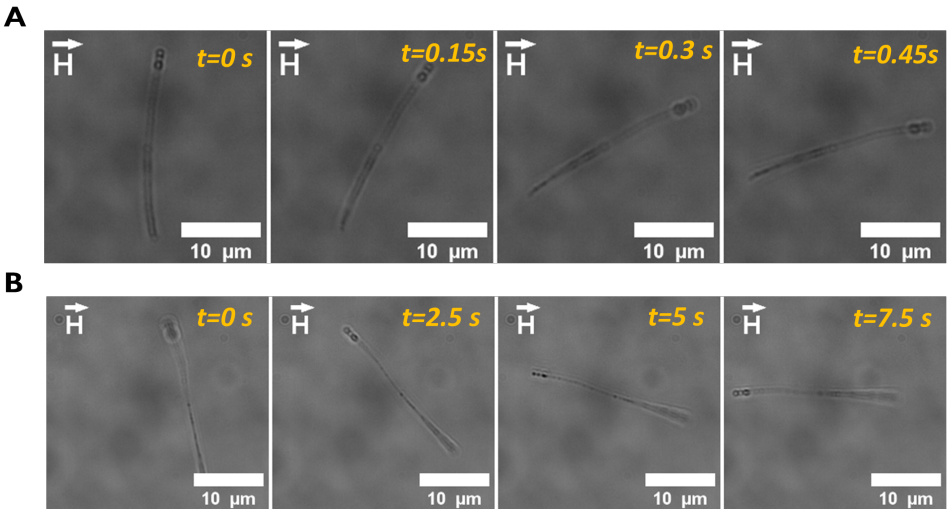

Fig. A4 Time series of optical images of functionalized BNNTs under horizontal magnetic field. (a) At field strength of H=240G, the nanotube rotates into alignment in less than 0.5s, **(b)** For the same nanotube, when field strength is H=43G, alignment into field direction takes ∼7.5 s

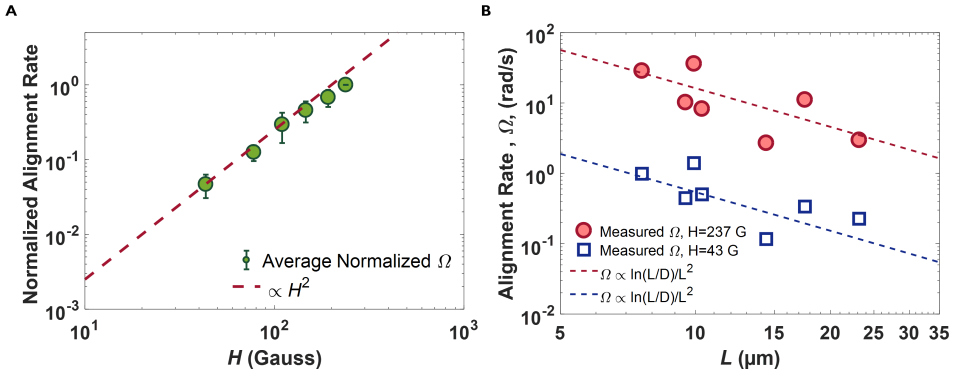

Fig. A5 Alignment of individual nanotubes under magnetic fields (a) Average normalized nanotube alignment rate of 7 BNNTs under different field strengths, nanotube rotation scales with H^2, **(b)** Nanotube alignment rate exhibits $ln(L/D)/L^2$ scaling with length for the highest and lowest applied field strengths. The deviation from the scaling line indicates a small inhomogeneity in the surface coverage with iron-oxide particles.

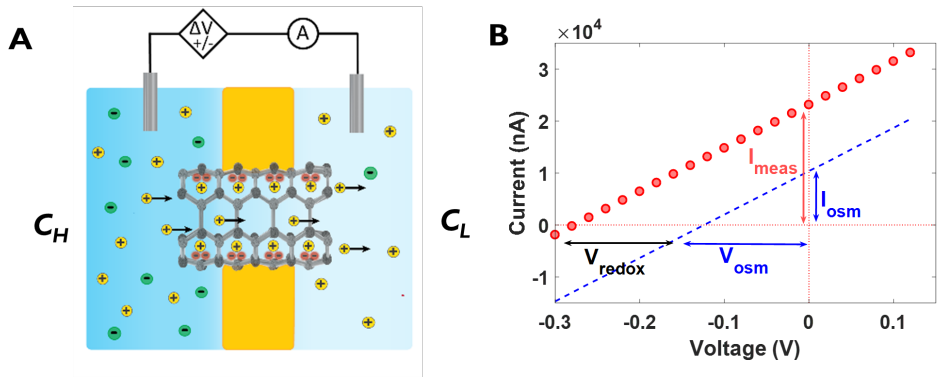

Fig. A6 **(a)** Experimental setup and current–voltage characteristics for a representative BNNT array in a 1mM:1M KCl gradient at pH=11. The contribution from the redox reaction on the electrodes (measured separately), is subtracted from the measured total current. **(b)** Representative $I-V$ curve for BNNT array showing measured values, and after subtraction of the redox potential.

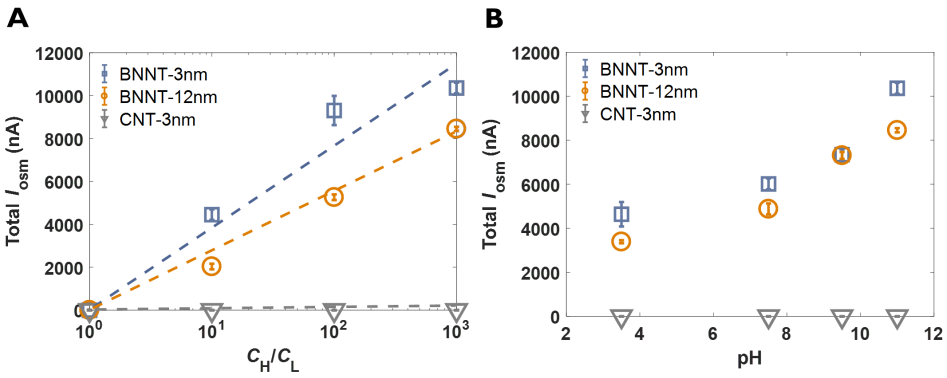

Fig. A7 **Measured osmotic currents for (a)** $C_H/C_L = 1000mM, 100mM, 10mM : 1mM$ KCl, at pH=11, **(b)** C_H/C_L =1M:1mM KCl, various pH solutions.

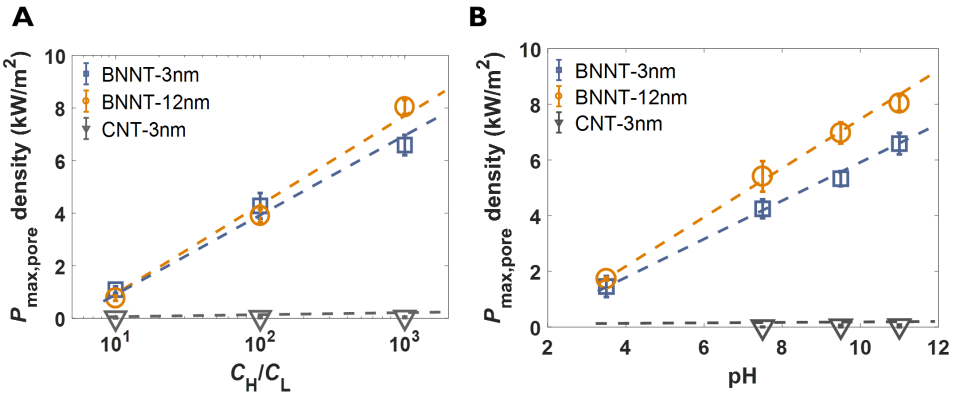

Fig. A8 Osmotic power generation densities for (a) $C_H/C_L = 1000mM, 100mM, 10mM$: $1mM$ KCl, at pH=11, **(b)** C_H/C_L =1M:1mM KCl, various pH solutions.

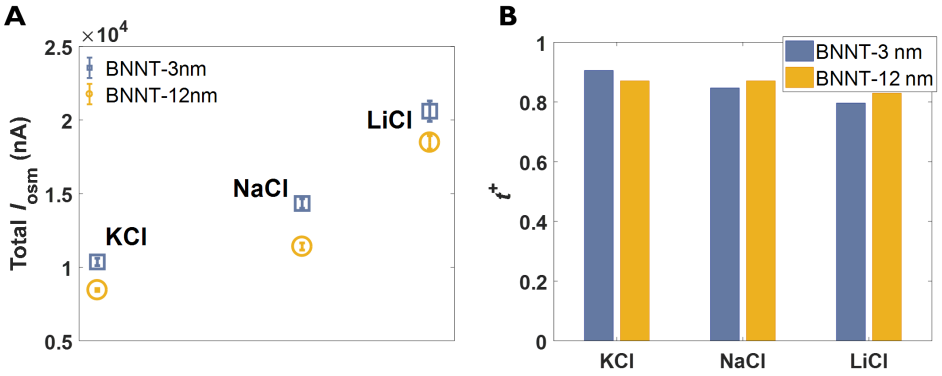

Fig. A9 (a) Measured osmotic currents of different cations for $C_H/C_L = 1000mM$: $1mM$, at pH=11, **(b)** Transference numbers for K^+, Na^+, Li^+ at C_H/C_L =1M:1mM, pH=11 solutions.

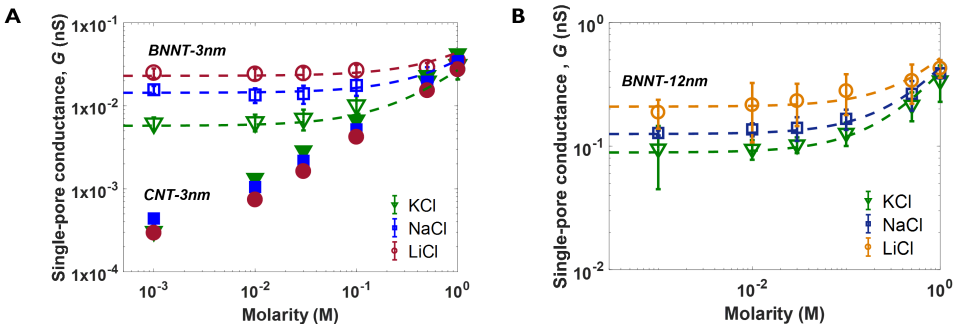

Fig. A10 **(a)** Comparison of ion conductance for CNT-3nm and BNNT-3nm with different cations, at pH=11, **(b)** Ion conductance of BNNT-12 nm arrays with different cations, at pH=11.

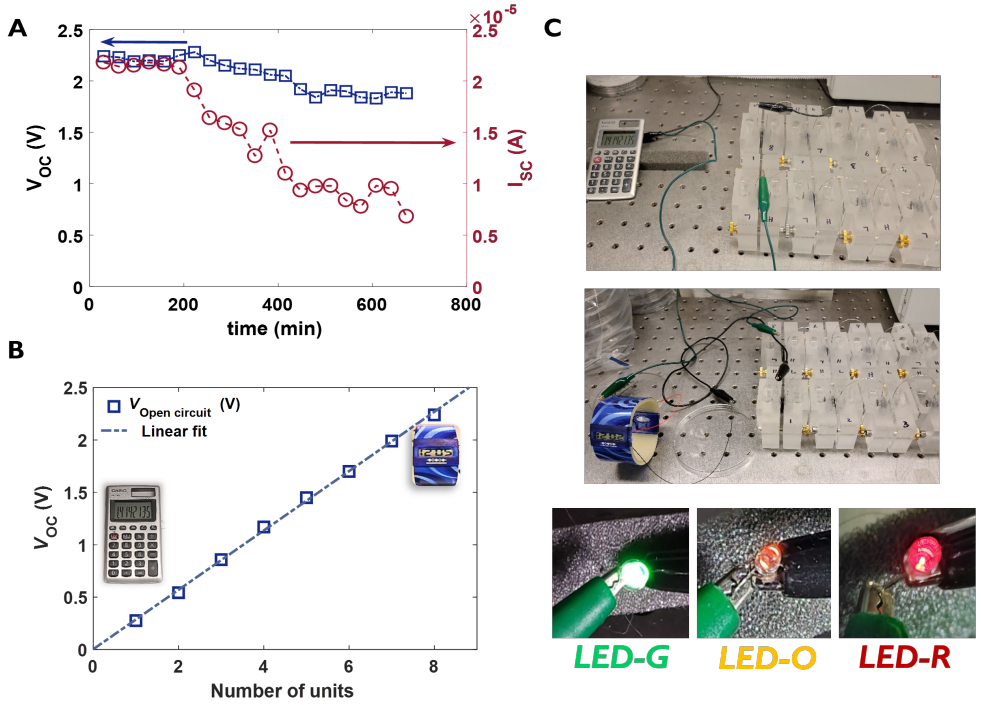

Fig. A11 **(a)** Open-circuit potential and short-circuit current over time, showing good stability for 4 hours, followed by a decrease for longer durations, **(b)** Open circuit potential by a stack of 8 BNNT arrays connected in series, **(c)** Powering of a calculator, a watch and LEDs with 8 BNNT arrays.

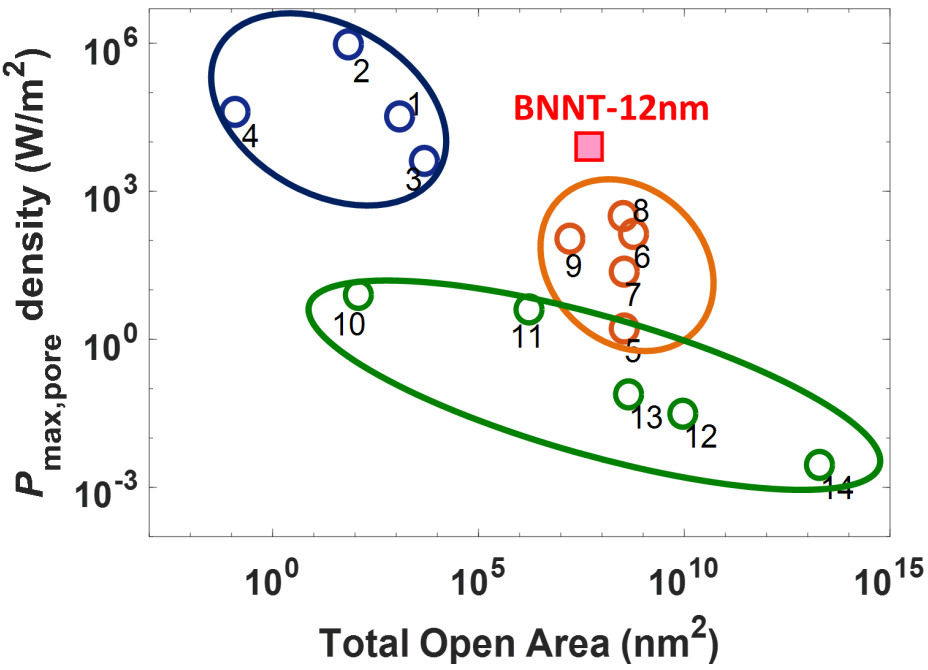

Fig. A12 **(a)** Maximum power density and total pore area for the BNNT arrays compared to other osmotic power generation systems. The blue circle highlights single-pore nanosystems, while the orange circle shows ionic-diode type heterogenous systems. The green circle shows state-of-the-art macroscopic membranes. Data and references are given in Table S??

References

[1] Sint, K., Wang, B., Král, P.: Selective ion passage through functionalized graphene nanopores. Journal of the American Chemical Society **130**, 16448–16449 (2008) https://doi.org/10.1021/ja804409f

[2] Rollings, R.C., Kuan, A.T., Golovchenko, J.A.: Ion selectivity of graphene nanopores. Nature Communications **7**, 1–7 (2016) https://doi.org/10.1038/ncomms11408

[3] Feng, J., Graf, M., Liu, K., Ovchinnikov, D., Dumcenco, D., Heiranian, M., Nandigana, V., Aluru, N.R., Kis, A., Radenovic, A.: Single-layer mos2 nanopores as nanopower generators. Nature **536**, 197–200 (2016) https://doi.org/10.1038/nature18593

[4] Graf, M., Lihter, M., Unuchek, D., Sarathy, A., Leburton, J.P., Kis, A., Radenovic, A.: Light-enhanced blue energy generation using mos2 nanopores. Joule **3**, 1549–1564 (2019) https://doi.org/10.1016/j.joule.2019.04.011

[5] Duan, C., Majumdar, A.: Anomalous ion transport in 2-nm hydrophilic nanochannels. Nature Nanotechnology **5**, 848–852 (2010) https://doi.org/10.1038/nnano.2010.233

[6] Gopinadhan, K., Hu, S., Esfandiar, A., Lozada-Hidalgo, M., Wang, F.C., Yang, Q., Tyurnina, A.V., Keerthi, A., Radha, B., Geim, A.K.: Complete steric exclusion of ions and proton transport through confined monolayer water. Science **363**, 145–148 (2019) https://doi.org/10.1126/science.aau6771

[7] Siria, A., Bocquet, M.-l., Bocquet, L.: New avenues for the large-scale harvesting of blue energy. Nature Reviews Chemistry **1**, 0091 (2017) https://doi.org/10.1038/s41570-017-0091

[8] Tunuguntla, R.H., Henley, R.Y., Yao, Y.-C., Pham, T.A., Wanunu, M., Noy, A.: Enhanced water permeability and tunable ion selectivity in subnanometer carbon nanotube porins. Science **357**, 792–796 (2017) https://doi.org/10.1126/science.aan2438

[9] Liu, H., He, J., Tang, J., Liu, H., Pang, P., Cao, D., Krstic, P., Joseph, S., Lindsay, S., Nuckolls, C.: Translocation of single-stranded dna through single-walled carbon nanotubes. Science **327**, 64–67 (2010) https://doi.org/10.1126/science.1181799

[10] Buchsbaum, S.F., Jue, M.L., Sawvel, A.M., Chen, C., Meshot, E.R., Park, S.J., Wood, M., Wu, K.J., Bilodeau, C.L., Aydin, F., Pham, T.A., Lau, E.Y., Fornasiero, F.: Fast permeation of small ions in carbon nanotubes. Advanced Science **8**, 2001802 (2021) https://doi.org/10.1002/advs.202001802

[11] Tunuguntla, R.H., Allen, F.I., Kim, K., Belliveau, A., Noy, A.: Ultrafast proton transport in sub-1-nm diameter carbon nanotube porins. Nature Nanotechnology **11**, 639–644 (2016) https://doi.org/10.1038/nnano.2016.43

[12] Král, P., Wang, B.: Material drag phenomena in nanotubes. Chemical Reviews **113**, 3372–3390 (2013) https://doi.org/10.1021/cr200244h

[13] Siria, A., Poncharal, P., Biance, A.L., Fulcrand, R., Blase, X., Purcell, S.T., Bocquet, L.: Giant osmotic energy conversion measured in a single transmembrane boron nitride nanotube. Nature **494**, 455–458 (2013) https://doi.org/10.1038/nature11876

[14] Brown, M.S., Shan, J.W., Lin, C., Zimmermann, F.M.: Electrical polarizability of carbon nanotubes in liquid suspension. Applied Physics Letters **90**, 203108 (2007) https://doi.org/10.1063/1.2740186

[15] Castellano, R.J., Praino, R.F., Meshot, E.R., Chen, C., Fornasiero, F., Shan, J.W.: Scalable electric-field-assisted fabrication of vertically aligned carbon nanotube membranes with flow enhancement. Carbon **157**, 208–216 (2020) https:

//doi.org/10.1016/j.carbon.2019.10.012

[16] Cetindag, S., Tiwari, B., Zhang, D., Yap, Y.K., Kim, S., Shan, J.W.: Surface-charge effects on the electro-orientation of insulating boron-nitride nanotubes in aqueous suspension. Journal of Colloid and Interface Science **505**, 1185–1192 (2017) https://doi.org/10.1016/j.jcis.2017.05.073

[17] Grosjean, B., Pean, C., Siria, A., Bocquet, L., Vuilleumier, R., Bocquet, M.L.: Chemisorption of hydroxide on 2d materials from dft calculations: Graphene versus hexagonal boron nitride. Journal of Physical Chemistry Letters **7**, 4695–4700 (2016) https://doi.org/10.1021/acs.jpclett.6b02248

[18] Grosjean, B., Bocquet, M.-L., Vuilleumier, R.: Versatile electrification of two-dimensional nanomaterials in water. Nature Communications **10**, 1656 (2019) https://doi.org/10.1038/s41467-019-09708-7

[19] Secchi, E., Niguès, A., Jubin, L., Siria, A., Bocquet, L.: Scaling behavior for ionic transport and its fluctuations in individual carbon nanotubes. Physical Review Letters **116**, 154501 (2016) https://doi.org/10.1103/PhysRevLett.116.154501

[20] Kim, D.K., Duan, C., Chen, Y.F., Majumdar, A.: Power generation from concentration gradient by reverse electrodialysis in ion-selective nanochannels. Microfluidics and Nanofluidics **9**, 1215–1224 (2010) https://doi.org/10.1007/s10404-010-0641-0

[21] Fornasiero, F., Park, H.G., Holt, J.K., Stadermann, M., Grigoropoulos, C.P., Noy, A., Bakajin, O.: Ion exclusion by sub-2-nm carbon nanotube pores. Proceedings of the National Academy of Sciences **105**, 17250–17255 (2008) https://doi.org/10.1073/pnas.0710437105

[22] Gadaleta, A., Sempere, C., Gravelle, S., Siria, A., Fulcrand, R., Ybert, C., Bocquet, L.: Sub-additive ionic transport across arrays of solid-state nanopores. Physics of Fluids **26**, 012005 (2014) https://doi.org/10.1063/1.4863206

[23] Sahu, S., Ventra, M.D., Zwolak, M.: Dehydration as a universal mechanism for ion selectivity in graphene and other atomically thin pores. Nano Letters **17**, 4719–4724 (2017) https://doi.org/10.1021/acs.nanolett.7b01399

[24] Esfandiar, A., Radha, B., Wang, F.C., Yang, Q., Hu, S., Garaj, S., Nair, R.R., Geim, A.K., Gopinadhan, K.: Size effect in ion transport through angstrom-scale slits. Science **358**, 511–513 (2017) https://doi.org/10.1126/science.aan5275

[25] Abraham, J., Vasu, K.S., Williams, C.D., Gopinadhan, K., Su, Y., Cherian, C.T., Dix, J., Prestat, E., Haigh, S.J., Grigorieva, I.V., Carbone, P., Geim, A.K., Nair, R.R.: Tunable sieving of ions using graphene oxide membranes. Nature Nanotechnology **12**, 546–550 (2017) https://doi.org/10.1038/nnano.2017.21

[26] Dove, P.M., Craven, C.M.: Surface charge density on silica in alkali and alkaline earth chloride electrolyte solutions. Geochimica et Cosmochimica Acta **69**, 4963–4970 (2005) https://doi.org/10.1016/j.gca.2005.05.006

[27] Emmerich, T., Vasu, K.S., Niguès, A., Keerthi, A., Radha, B., Siria, A., Bocquet, L.: Enhanced nanofluidic transport in activated carbon nanoconduits. Nature Materials **21**, 696–702 (2022) https://doi.org/10.1038/s41563-022-01229-x

[28] Kramers, H.A.: Brownian motion in a field of force and the diffusion model of chemical reactions. Physica **7**, 284–304 (1940) https://doi.org/10.1016/S0031-8914(40)90098-2

[29] Mazo, R.M.: Brownian Motion: Fluctuations, Dynamics, and Applications. Oxford University Press, New York (2002)

[30] Zhang, Z., Wen, L., Jiang, L.: Nanofluidics for osmotic energy conversion. Nature Reviews Materials **6**, 622–639 (2021) https://doi.org/10.1038/s41578-021-00300-4

[31] Vermaas, D.A., Veerman, J., Yip, N.Y., Elimelech, M., Saakes, M., Nijmeijer, K.: High efficiency in energy generation from salinity gradients with reverse electrodialysis. ACS Sustainable Chemistry Engineering **1**, 1295–1302 (2013) https://doi.org/10.1021/sc400150w

[32] Pendse, A., Cetindag, S., Rehak, P., Behura, S., Gao, H., Nguyen, N.H.L., Wang, T., Berry, V., Král, P., Shan, J., Kim, S.: Highly efficient osmotic energy harvesting in charged boron-nitride-nanopore membranes. Advanced Functional Materials **31**, 2009586 (2021) https://doi.org/10.1002/adfm.202009586

[33] Holt, J.K., Park, H.G., Wang, Y., Stadermann, M., Artyukhin, A.B., Grigoropoulos, C.P., Noy, A., Bakajin, O.: Fast mass transport through sub-2-nanometer carbon nanotubes. Science **312**, 1034–1037 (2006) https://doi.org/10.1126/science.1126298

[34] Yang, D.-C., Castellano, R.J., Silvy, R.P., Lageshetty, S.K., Praino, R.F., Fornasiero, F., Shan, J.W.: Fast water transport through subnanometer diameter vertically aligned carbon nanotube membranes. Nano Letters **23**(11), 4956–4964 (2023) https://doi.org/10.1021/acs.nanolett.3c00797

[35] Erb, R.M., Libanori, R., Rothfuchs, N., Studart, A.R.: Composites reinforced in three dimensions by using low magnetic fields. Science **335**, 199–204 (2012) https://doi.org/10.1126/science.1210822

[36] Arcenegui, J.J., García-Sánchez, P., Morgan, H., Ramos, A.: Electro-orientation and electrorotation of metal nanowires. Physical Review E **88**, 063018 (2013) https://doi.org/10.1103/PhysRevE.88.063018

[37] Grenadier, S., Li, J., Lin, J., Jiang, H.: Dry etching techniques for active devices based on hexagonal boron nitride epilayers. Journal of Vacuum Science Technology A: Vacuum, Surfaces, and Films **31**, 061517 (2013) https://doi.org/10.1116/1.4826363

[38] Fröch, J.E., Hwang, Y., Kim, S., Aharonovich, I., Toth, M.: Photonic nanostructures from hexagonal boron nitride. Advanced Optical Materials **7**, 1801344 (2019) https://doi.org/10.1002/adom.201801344